

## Transport matrices from standard ocean-model output and quantifying circulation response to climate change

Matthew A. Chamberlain<sup>\*,a</sup>, Richard J. Matear<sup>a</sup>, Mark Holzer<sup>b</sup>, Daohua Bi<sup>c</sup>, Simon J. Marsland<sup>c</sup>

<sup>a</sup> CSIRO, Castray Esplanade, Hobart TAS Australia

<sup>b</sup> School of Mathematics and Statistics, University of New South Wales, Sydney NSW, Australia

<sup>c</sup> CSIRO, Aspendale VIC, Australia

### ARTICLE INFO

#### Keywords:

Transport matrix  
Ocean ventilation  
Global ocean modelling  
Tracers  
Ideal mean age

### ABSTRACT

A method to construct transport matrices from standard ocean-model output, such as mean volume fluxes and mixed-layer depths, is presented. These transport matrices enable highly efficient calculation of deep-water tracer fields that otherwise require long integrations with forward time-stepping ocean models. Comparisons of matrix solutions for ideal mean water age demonstrate that the transport matrices are reasonably accurate representations of the transport in the parent ocean models.

Tracer fields calculated using transport matrices provide simple circulation metrics that can be compared to observations. We compare matrix-computed radiocarbon distributions from two versions of ACCESS ocean models with observations. We find matrices based on both models produce realistic circulations; the radiocarbon distribution based on ACCESS forced with CORE climatology fits observations better in the deep Pacific, whereas the fully coupled ACCESS1.3 model fits observations better in the deep Atlantic.

When applied to the circulations of ACCESS1.3 climate-change experiments, the transport-matrix solutions show an increase in radiocarbon depletion, or water age, in the projected ocean circulation for the 2090s under the RCP8.5 scenario. By computing the water-mass fractions last ventilated from specific regions, we diagnose a corresponding progressive shutdown in Antarctic Bottom Water formation. The volumetric decrease in Antarctic waters in the global ocean is compensated by an increase in waters last ventilated in the subantarctic and southern subtropics.

### 1. Introduction

The oceans have the capacity to store and release huge amounts of heat and carbon, making them an important component of the climate system. The deep ocean circulation is crucial to the modulation of the earth's climate on centennial and longer timescales (Rhein et al., 2013). Natural radiocarbon has provided important insights into the deep ocean circulation and simulations of natural radiocarbon provide a valuable way to assess the simulated deep ocean ventilation (e.g., Toggweiler et al., 1989a; 1989b). However, it takes many millennia for the deep-ocean natural radiocarbon to reach steady state. Therefore, numerical ocean general circulation models (OGCM) need long integration times, which is computationally expensive.

There are several ways to reduce the computational requirements to equilibrate passive tracers. One approach is to use an off-line version of the OGCM in which tracers are advected and diffused from archived circulation output of the OGCM (Ribbe and Tomczak, 1997). While this

allows the use of somewhat longer time steps, the computational expense is still very large. A second approach is to initialise the model with an initial state closer to equilibrium by integrating a coarse-resolution offline model, that is much more efficient to integrate (Aumont et al., 1998). A third approach is to use a transport matrix built from an OGCM to represent the advection-diffusion operator (Khatiwala et al., 2005; Khatiwala, 2008).

The attraction of the matrix transport method is that it provides a highly efficient way to solve the steady-state distributions of passive tracers and many transport diagnostics. For example, DeVries and Primeau (2011) used a data-assimilated transport matrix derived from observations of temperature, salinity, radiocarbon, sea-surface height and buoyancy fluxes, to calculate the fractions of the interior ocean volume that were last ventilated in specified surface regions such as the Southern Ocean and North Atlantic. The transport matrix can also be used to determine surface-to-surface and surface-to-interior pathways (e.g., Primeau, 2005; Holzer and Primeau, 2006; 2008; Gebbie and

\* Corresponding author.

E-mail address: [matthew.chamberlain@csiro.au](mailto:matthew.chamberlain@csiro.au) (M.A. Chamberlain).

Huybers, 2010). Finally, the transport matrix also allows for highly efficient formulations of biogeochemical models so that their parameters can be objectively analysed, for example, the phosphate cycle (Kwon and Primeau, 2006; Primeau et al., 2013; Holzer and Primeau, 2013; Fu and Primeau, 2017), silicon cycle (Holzer et al., 2014; Holzer and Brzezinski, 2015), iron cycles (Frants et al., 2016; Pasquier and Holzer, 2017) and radiocarbon (Bardin et al., 2014).

Here, we use the transport-matrix approach to find the steady-state solutions for water age, natural radiocarbon, and to map constituent water masses according to regions of their last-ventilation. The transport matrix representing an ocean's advection-diffusion operator for a given circulation can be constructed using several different techniques. The matrix can be built with injected tracer pulses at each grid point and using resulting output to construct the underlying advection-diffusion operator (Khatiwala et al., 2005). Here, we use an approach analogous to Primeau (2005) where the saved mean advective transports (eulerian and eddy components), diffusivities (horizontal and vertical) and upper ocean mixed-layer depths are used to build the transport matrix. We use time means of archived circulation fields from selected decades for this purpose.

The layout of the paper is as follows. Section 2 describes the parent OGCMs and the construction of the transport matrices from the OGCM archived circulation. We show that the transport matrix produces good representations of ideal mean water ages simulated directly with the OGCMs. In Section 3, we use the transport matrix to compute the steady-state radiocarbon field and water-mass fractions. We then build transport matrices for different climate simulations to quantify how the deep ocean circulation and ventilation change between the pre-industrial and the projected RCP8.5 climates.

## 2. Method

### 2.1. Models used

#### 2.1.1. Ocean-ice model

The longest forward-model integration for this project was an ocean-only configuration of the Australia Community Climate Earth System Simulator (ACCESS), which was run for 1000's of years. The model is based on Bi et al. (2013), using the same ocean model (MOM4p1, Griffies, 2008), grid, and ocean parameters. The sea ice model in this experiment is the Sea Ice Simulator, as used in GFDL's Climate Model (CM2.1, Delworth et al., 2006). The ACCESS grid is spherical over most of the globe with 1-degree resolution in longitude. Latitude resolution varies; resolution is  $0.33^{\circ}$  within  $10^{\circ}$  of the Equator, increasing to  $1^{\circ}$  at  $30^{\circ}$  North and South. South of  $30^{\circ}$ , the resolution is Mercator, becoming  $0.25^{\circ}$  at  $75^{\circ}$  S. A tripolar grid over the Arctic is used to avoid the North Pole singularity. The long integration was forced with atmospheric reanalysis fields used in the Coordinated Ocean Reference Experiment (CORE, Griffies et al., 2009). Vertical resolution is 10 m in the upper 200 m and 300 m at the maximum depth of 5000 m. The vertical coordinates are "zstar," which scale with surface height in time. The upper ocean is mixed with the K-profile parameterisation (KPP) scheme and vertical background diffusivity of  $2 - 2.5 \times 10^{-5} \text{ m}^2 \text{s}^{-1}$  (higher values near poles), the biharmonic friction scheme is used and neutral physics includes Redi diffusivity ( $600 \text{ m}^2 \text{s}^{-1}$ ) and Gent-McWilliams skew diffusion.

#### 2.1.2. Atmosphere-ocean-ice model

Matrices are also built with output from ACCESS Coupled Model version 1.3 (ACCESS1.3) experiments submitted to the Coupled Model Intercomparison Project (CMIP), phase 5 (Bi et al., 2013). The set up of the ocean model is the same as the ocean-only model described above, and is coupled to the Los Alamos sea ice model (CICE, version 4.1, e.g. Flocco et al., 2012). The atmospheric component of ACCESS1.3 is the Unified Model (UM, version 7.3) from the Met Office (Hadgem2 Development Team et al., 2011). In this work, we have produced

several matrices based on the ACCESS1.3 historical and RCP8.5 scenarios. Time-independent matrices are built on decadal averages of circulation to minimise any impact of year-to-year variability; decades used are 1890–1899, 1990–1999, 2040–2049 and 2090–2099.

### 2.2. Matrix construction and evaluation

The following subsections firstly discuss the application of the transport matrices to solving steady-state distributions of ocean tracer fields. The mean water age tracer in particular is presented, for which a steady-state solution was also found with the forward ocean model for comparison. The next subsections describe the construction of the transport matrices used here, the results of which are compared to the forward model. Extra details regarding the matrix construction may be found in the appendix.

#### 2.2.1. Matrix formulation

In this method, a tracer field in the ocean is represented as a vector,  $\chi$  (an array of  $\sim 2.6 \times 10^6$  values for ACCESS ocean models). The time tendency of this tracer due to physical advection, eddy diffusion and vertical mixing is given by  $A\chi$ , where  $A$  is the discretised advection-diffusion operator organised into a matrix.  $A$  is what we refer to as the transport matrix, a very sparse matrix with  $\sim 2 \times 10^7$  non-zero elements (representing  $\sim 0.0003\%$  of the total entries, corresponding to exchanges between nearest neighbours in the "real" ocean). The time tendency of the tracer becomes

$$\frac{d}{dt}\chi = A\chi + b, \quad (1)$$

where  $b$  is a vector form of tracer sources and sinks. When  $b$  is a constant vector, the steady-state solution ( $A\chi = -b$ ) is solved via standard matrix methods (essentially LU factorisation followed by back substitution, often loosely referred to as "matrix inversion"). We used the Pardisio sparse matrix package within the Intel Math Kernel Library to solve this linear system.

If the sources and/or sinks  $b$  depend nonlinearly on the tracer concentration  $\chi$ , then Eq. 1 becomes, after discretisation onto the numerical grid, a system of non-linear coupled algebraic equations. This occurs, for example, for nutrient tracers whose biological sink in the upper ocean ("uptake") can be represented with a Monod limiting term of the form  $\frac{\chi}{\chi+k}$ , where  $k$  is constant. In such nonlinear cases, Eq. 1 can still be solved efficiently by, for example, Newton solvers (Pasquier and Holzer, 2017). These solvers typically converge in of the order of 10 steps, a vast improvement in the computational efficiency over time-stepping a forward model to find the steady state. Here, we only consider linear tracers, specifically ideal mean water age, water-mass fractions, and radiocarbon, as detailed below.

#### 2.2.2. Water age and forward model solutions

Water age tracer fields are readily calculated from transport matrices and can be compared to age tracers from forward models to assess how well matrices simulate the forward model circulation, particularly in the deep ocean. Solving for the steady-state solution involves applying the boundary condition that water age at the ocean surface is zero and a uniform age "source" of one second per second in the ocean interior. Since the source vector,  $b$ , is constant, the solution can be found by a single matrix inversion.

Fig. 1 shows water age trends in the "deep North Pacific" (defined here as the average from  $160 - 220^{\circ}\text{E}$ ,  $20 - 60^{\circ}\text{N}$  and below 2000 m), representing part of the ocean with the longest timescale. Several water age tracer trends are shown here, initialised from solutions of various matrices (discussed below) and integrated forward in time with the parent ocean model. The physical circulation of the ocean model had already been spun up for  $\sim 1000$  years. In each case, the age tracer converges towards a common state within the forward model, regardless of initial condition, as expected.

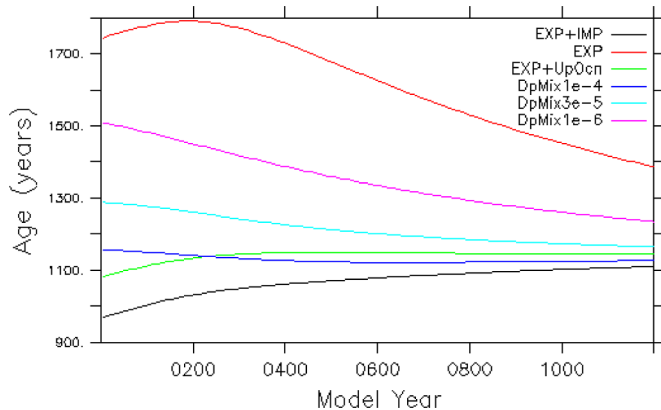


**Fig. 1.** Evolution of deep North Pacific water ages (average within 160 – 220°E, 20 – 60°N and below 2000 m), initialised from various matrix solutions (see Sections 2.2.2 and 2.2.4 for details) and integrated in the parent forward ocean model towards a stable solution.

Some age tracer trends shown in Fig. 1 were initialised with solutions from matrices constructed with a specialised “transport\_matrix” tracer package available in the MOM4p1 release (Khatiwala et al., 2005; Griffies, 2008). This tracer package uses unique “puff” tracers at every grid point and every time step to extract transport matrix elements, calculating separate matrices for explicit and implicit processes. It is important to note, however, this package is different to the method to construct matrices described and used in the following sections. Also shown in Fig. 1 are lines labelled “DpMixXX,” which are age trends initialised with matrices that are described in following sections.

The range of tracer fields in Fig. 1 include initialisations that both under- and overestimate the final state of the ocean model’s age tracer, but all converge to the same age and are shown here just for demonstration. The solution from only explicit processes (“EXP”) has no vertical mixing and overestimated deep water ages, while including vertical, implicit mixing (“EXP + IMP”) underestimated water ages. The low age bias of the “EXP + IMP” solution is consistent with the results of Bardin et al. (2016) who found that ages derived from annual averages of transport were younger by ~12% relative to ages found with better temporal resolution. A matrix combining the explicit matrix with well-mixed upper oceans (“EXP + UpOcn”) produced an initial state that resulted in the least drift after 1000+ years of forward integration. This case was integrated a further 1000 years and is used as the “forward solution” of the water age for the ocean model and a reference for matrix solutions. The drift in the deep North Pacific ages of this integration was less than 3 years over this 1000 years. Integrating this tracer an extra 1000 years had negligible effect on the correlations listed below (changes were in the 3rd significant figure).

Correlations and deep water ages from various matrix age solutions are compared in Table 1 and the Taylor diagram in Fig. 2. Matrices “EXP + IMP” and “EXP + UpOcn” produce reasonable correlations (0.960 and 0.948 respectively, Table 1), indicating these matrices give a

good representation of the parent ocean models circulation. However, these matrices can only be constructed from experiments with specialised transport matrix tracers. Other solutions listed in Table 1 (“DpMixXX”) are constructed using generic ocean-model output such as water transport and mixed-layer depth as described below.

### 2.2.3. Advection

Time tendencies of tracers due to advection from neighbouring cells could be calculated from ocean model velocities. However, using volume transports is preferable since these include effects from changes in sea level and partial cells in the ocean model affecting tracer advection. Archived horizontal volume transports are used, vertical transports are calculated from the divergence of the horizontal components to ensure volume conservation. Eddy-induced transports from the Gent-McWilliams component of the neutral physics scheme are also included. In summary, the time tendency of a tracer due to advection from neighbouring cells is the average volume transport from that neighbour, normalised by the cell volume. Similarly, transports out of the cell are loss terms. The Appendix A has a schematic of the tracer grid and fluxes, and Eq. A. 2 that demonstrate the terms used to calculate the advective components of the transport matrix.

The matrix built with just these diagnosed transports produces an age solution that has a reasonable correlation with the forward solution (“advection-only” in Table 1,  $R=0.931$ ). However, this solution also has the oldest of the water ages shown since this matrix is missing various ocean model subgrid processes, reducing the connection of the ocean interior to the surface and increasing the water age.

### 2.2.4. Vertical and horizontal mixing

A matrix of tracer mixing is added to the advection matrix above to improve deep ocean solutions. Tracer exchange by mixing is calculated vertically and horizontally just between neighbouring tracer cells, using grid information such as displacement and interface areas between cells. See Appendix A for a schematic and equation showing the various terms. The ocean is divided into two regions for vertical mixing; a well-mixed upper ocean, and a deep ocean with background mixing. Uniform diffusion coefficients are applied in these regions. The depth of the upper ocean here is defined by the maximum in seasonal mixed-layer depths from corresponding forward ocean model experiments, and varies spatially from a few tens of metres to a few hundred metres in the tropics and midlatitudes. In high latitudes, there are regions of deep mixing to several hundred metres along the subantarctic zone and in the North Atlantic, and locations with mixing to over 1000 m in Antarctic seas. Uniform horizontal mixing is included as a simplified approximation for isopycnal mixing.

Ideal mean water age solutions with various components of ocean circulation and mixing are compared to the forward solution in Table 1 and shown in Fig. 2a. The biggest improvement from the advection-only solution comes from the inclusion of upper ocean vertical mixing, which improves both the correlation ( $R$ ) and reduces the age to be closer to the forward solution, consistent with the importance of

**Table 1**

Correlations of age solutions from various matrix constructions shown in Fig. 2a, and solutions used as initial conditions in Fig. 1.

Label (Fig. 2a)	Correlation	Deep North Pacific Age	Matrix Construction
1	1.000	1145.	reference forward model
2	0.901	1743.	explicit-only
3	0.960	966.	explicit + implicit
4	0.948	1079.	explicit + upper ocean mixing
5	0.931	2187.	advection only
6	0.966	1410.	advection + upper ocean mixing
7	0.974	1407.	advection + upper and deep mixing
	0.943	1155.	advection + upper, deep(1e-4) and horiz. mix
8	0.977	1288.	advection + upper, deep(3e-5) and horiz. mix
	0.985	1507.	advection + upper, deep(1e-6) and horiz. mix

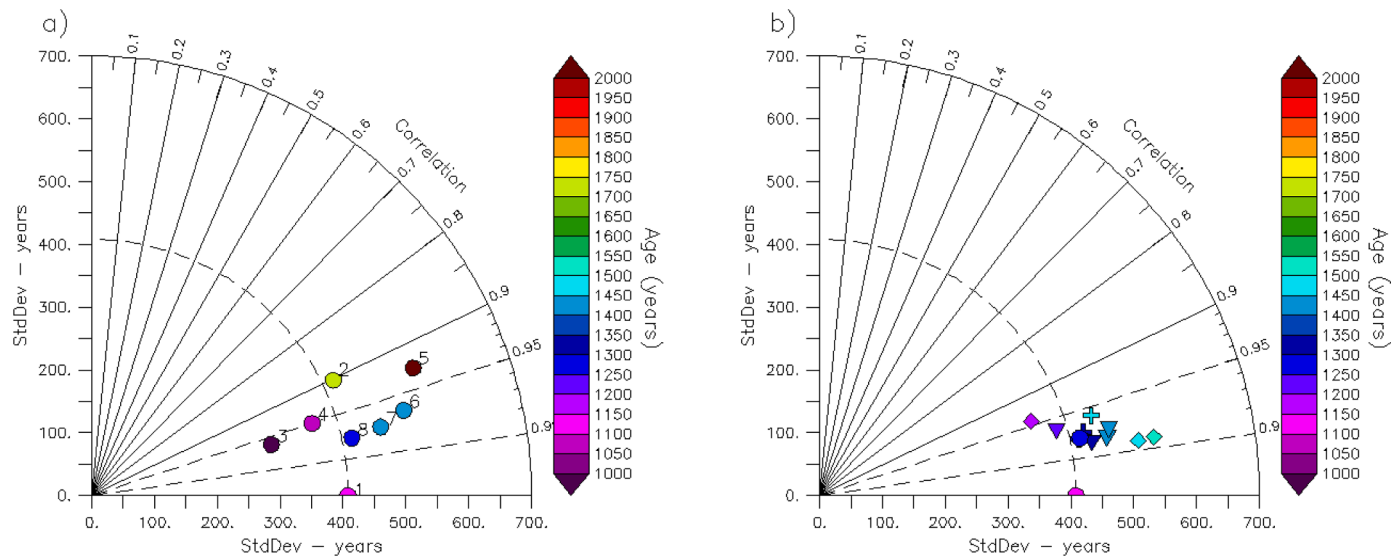


**Fig. 2.** Taylor diagrams of various water age solutions referenced to the forward solution. Colours represent the age of deep North Pacific waters. The left panel shows the effect of different matrix constructions (listed in Table 1) and the right panel shows effects of varying mixing parameters (see Section 2.2.4 for details).

vertical connections in major water formation regions in setting global tracer distributions. The inclusion of background diffusivity produces small improvements in both  $R$  and age; horizontal mixing substantially improves the age with a minor effect on  $R$ .

The values tested for tracer diffusivities were based on physically reasonable estimates and compared to the forward age solution. Fig. 2b compares solutions from various combinations of mixing parameters. Diamonds show the effect of varying deep ocean background diffusivity ( $10^{-4} - 10^{-6} \text{ m}^2\text{s}^{-1}$ ). Triangles show different horizontal eddy diffusivity ( $10^2 - 10^3 \text{ m}^2\text{s}^{-1}$ ). Crosses are results from a range of upper ocean mixing ( $0.001 - 1.0 \text{ m}^2\text{s}^{-1}$ ). The circle is the solution using “preferred” diffusivity values (upper mixing  $0.1 \text{ m}^2\text{s}^{-1}$ , deep diffusivity  $3 \times 10^{-5} \text{ m}^2\text{s}^{-1}$ , and horizontal mixing  $5 \times 10^2 \text{ m}^2\text{s}^{-1}$ ). For diffusivity values explored here, increasing vertical mixing in deep water decreases the mean water age in the deep North Pacific and the standard deviation. The best  $R$  values are found with small deep mixing diffusivities, though the associated water ages are substantially greater and solutions plot further away from the reference point on the Taylor diagram. The deep water vertical mixing value is also close to the background mixing of the forward model ( $2 - 2.5 \times 10^{-5} \text{ m}^2\text{s}^{-1}$ ). Increasing mixing in the upper ocean gives small improvements to  $R$ , which we use, but we also stay within a range of mixing coefficients diagnosed by the ocean model, of the order of  $0.1 \text{ m}^2\text{s}^{-1}$  in the upper ocean. Increasing horizontal mixing, or eddy-diffusivity, also reduces water ages and improves  $R$ ; however excessive horizontal mixing degrades the correlation. The value of horizontal mixing that gave the best solution from tuning in Fig. 2b is close to the neutral isopycnal diffusivity used in the ocean model experiment ( $600 \text{ m}^2\text{s}^{-1}$ ).

#### 2.2.5. Comparing matrix and forward model tracer fields

Various matrix-derived water age fields are compared in Fig. 3 to the forward solution (g, h). Without horizontal mixing (c, d), the solution shows small amplitude, high-frequency features that are unrealistic for deep ocean tracers. In Fig. 1, a solution with higher background mixing (DpMix1e-4, e and f) has a deep North Pacific age closer to the stable, forward solution than the preferred matrix (DpMix3e-5, a and b). However, this higher mixing solution has a lower correlation coefficient and is further from the reference solution in Fig. 2b. In Fig. 3e the depth of maximum age of DpMix1e-4 is deeper relative to

the forward solution. In the preferred solution (a, b), the oldest water is close to the correct age and has the right depth and extent, giving a better representation of the forward model circulation.

Fig. 4 shows a joint probability distribution of ideal water ages from the preferred matrix and the reference forward model. (The joint distribution can be thought of as a binned, volume-weighted scatter plot.) Most of the ocean falls close to the 1:1 line. There is a slight young bias ( $\sim 50$  years) in waters of intermediate age (400–600 years), whereas oldest waters, such as in the deep North Pacific, are biased old ( $\sim 50 - 100$  years). Some outliers occur, such as poorly connected parts of the Arctic Ocean which are younger in the matrix-derived field relative the forward model, and even the Mediterranean which is older in the matrix field. However, the age of most of the ocean volume is well represented in the matrix solution.

### 3. Comparing circulation of different models and climates

Using the structure of the preferred matrix found in Sections 2.2.3 and 2.2.4 (upper mixing  $0.1 \text{ m}^2\text{s}^{-1}$ , deep diffusivity  $3 \times 10^{-5} \text{ m}^2\text{s}^{-1}$ , and horizontal mixing  $5 \times 10^2 \text{ m}^2\text{s}^{-1}$ ), we now consider transport matrices constructed from transports and mixed-layer depths of other forward ocean model experiments testing different model setups and climate scenarios. These matrices are then used to calculate radiocarbon distributions which enable comparisons of these simulations and their tracers to observations. We also calculate the water volumes last ventilated in various regions (or water masses), and for various climate scenarios. Tracer distributions in the deep ocean are our primary interest.

#### 3.1. Radiocarbon

We now consider steady-state radiocarbon fields computed with transport matrices based on OGCM simulations of the contemporary climate. Fig. 5 compares the matrix-derived radiocarbon field for the ACCESS-ocean with CORE forcing (left column) and the ACCESS1.3 1990s (middle) with the GLODAP observations (right, Key et al., 2004). Water ages are less than the half-life of carbon-14 (5730 years), so the decay of carbon-14 is approximately linear on ocean timescales, hence the radiocarbon distribution is similar to water age fields shown before,

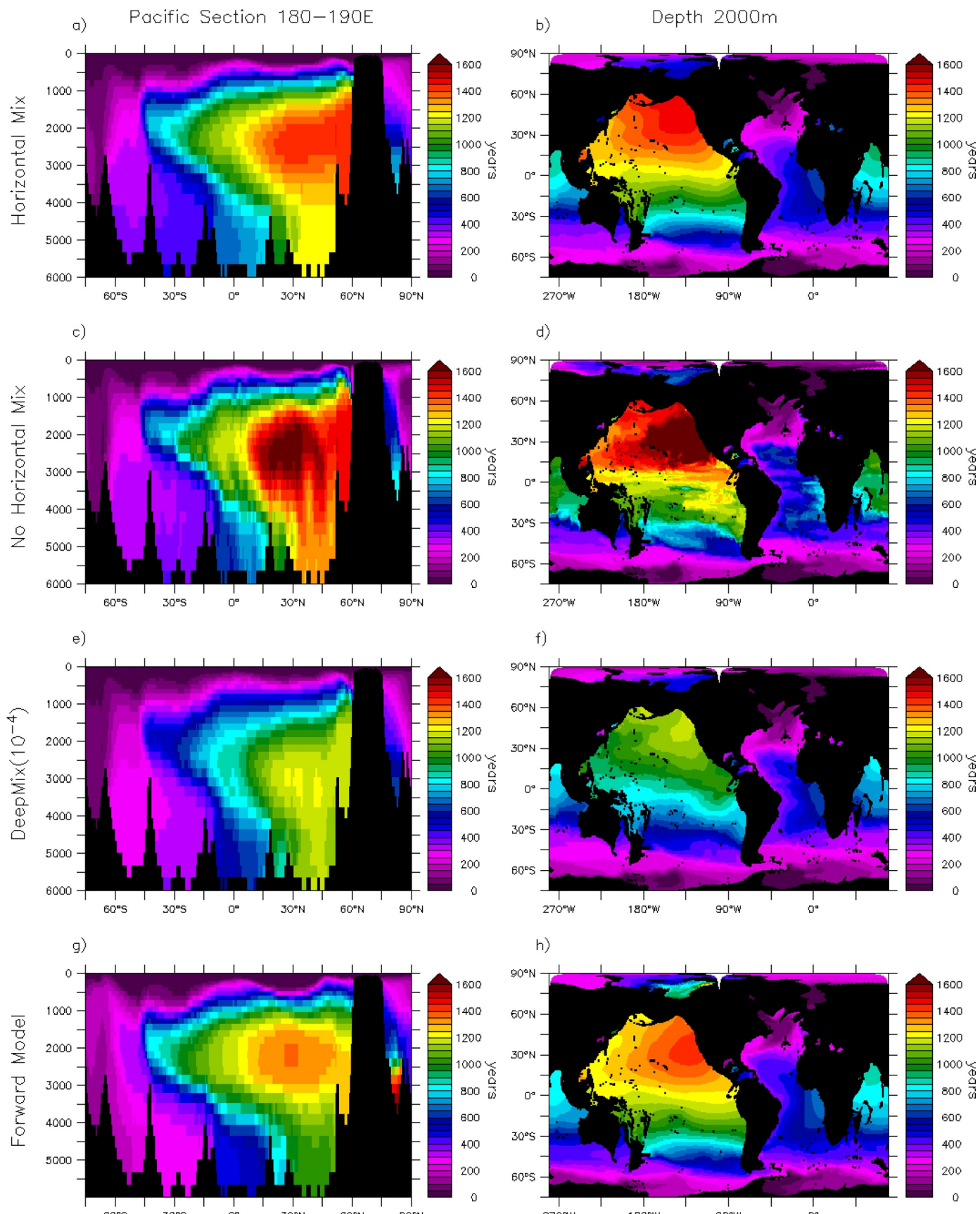


**Fig. 3.** Distributions of mean water age: preferred matrix solution (a, b; label 8 in Table 1), without horizontal mixing (c, d), higher vertical background mixing (e, f) and the forward solution (g, h). Left column shows Pacific sections of water age averaged over 180–190°E; right column shows water age at 2000 m depth.

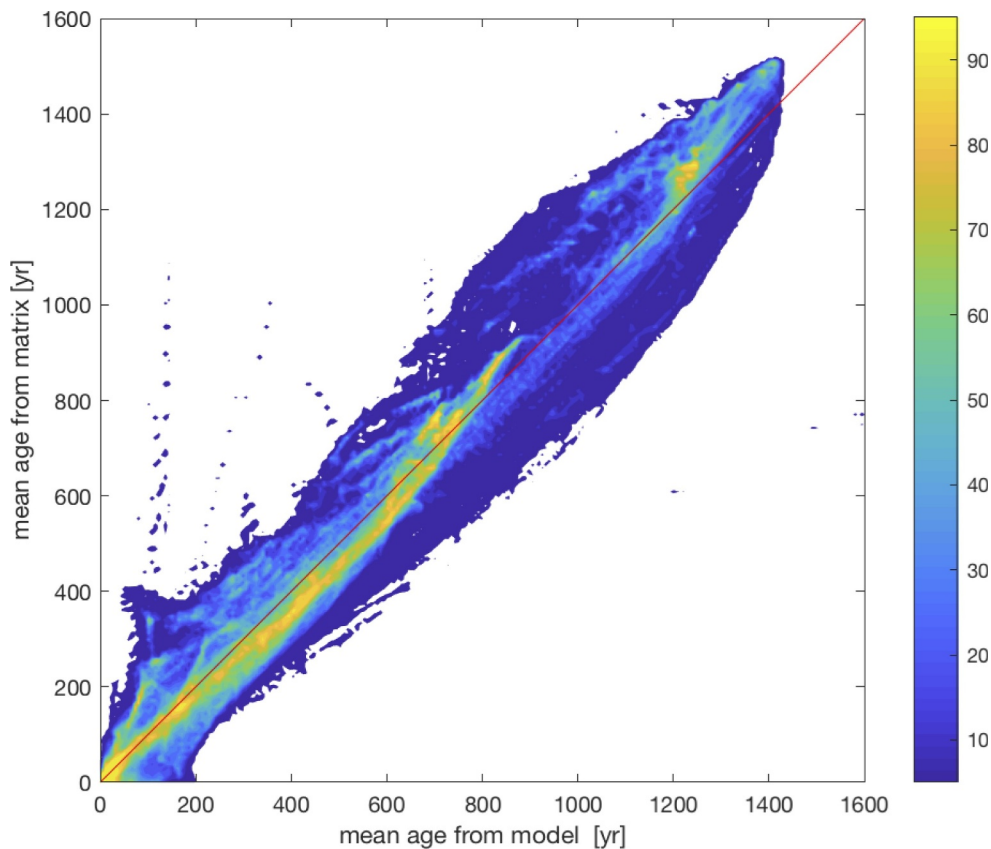


**Fig. 4.** Joint, cumulative volume-weighted distribution of mean water age from the matrix (vertical axis) and forward model (horizontal). The colourscale values are percentiles such that, for example, 90% of the ocean volume lies outside the “90” colour.

particularly in the deep ocean. Near the air-sea surface, however, radiocarbon is in disequilibrium; the equilibration time scales for radiocarbon is months to years for reasonable mixed-layer depths using exchange rates from Toggweiler et al. (1989a), whereas ideal age tracers equilibrate instantaneously. Ocean radiocarbon is shown in units of  $\Delta$ -carbon, which is the change in the isotope ratio of carbon-14 to carbon-12 per mil, relative to atmospheric values before nuclear weapons testing (Toggweiler et al., 1989a). Solving for the steady-state radiocarbon solution is similar to solving for water age described before. The surface boundary condition is the carbon-14:carbon-12 ratio taken from the GLODAP pre-bomb database (Key et al., 2004), and this ratio decays in the ocean interior with the carbon-14 half-life.

The overall structures of radiocarbon depletion in Fig. 5 from ACCESS-ocean and ACCESS1.3 experiments are similar. In the Pacific (top row), radiocarbon sections from both experiments are very similar to the observed radiocarbon; ACCESS-ocean radiocarbon is slightly more depleted (older) than observations, while ACCESS1.3 is less depleted (younger) and upper ocean waters penetrate deeper. There are small discrepancies between models and observations in the top few hundred metres. By assuming rapid mixing down to the winter maximum mixed-layer depths, modelled radiocarbon fields mix surface boundary conditions to depths of the order of 100 m. Observed radiocarbon has significant vertical gradients in the top few tens of metres due to disequilibrium across the air-sea surface and shallow average mixed layers. Both models show older water in the deep Southern Ocean and more bottom water penetration into the Pacific basin relative to the observations. In the Atlantic, ACCESS1.3 has a more realistic representation of North Atlantic Deep Water, whereas the ACCESS-ocean

has abyssal water pooling and ageing in the North Atlantic. The observed radiocarbon distribution also shows old, depleted waters in the abyssal South Atlantic which are not seen in model solutions. Models may be missing a connection of Pacific abyssal water into the Atlantic basin. However, further investigation of this feature is beyond the scope of this work.

### 3.2. Water-mass fractions

DeVries and Primeau (2011) use a data-constrained ocean circulation model, which assimilates observations of heat, salinity and radiocarbon tracers in addition to observed sea height and surface fluxes of heat and fresh water, and estimate the volume fraction of the ocean last ventilated in various surface regions. Here we calculate corresponding volume fractions using our model-derived transport matrices. Fig. 6 shows surface regions we use for this purpose. These regions were defined using the same criteria used by Gebbie and Huybers (2010) and DeVries and Primeau (2011). Antarctic and subantarctic water are separated by the  $1027.1 \text{ kg m}^{-3}$  isopycnal. The 35.0-psu isohaline divides subantarctic and subtropical waters. The tropical waters are within the  $25^\circ\text{C}$  isotherm. Subtropical and subarctic waters are separated by the 34.0-psu and 35.4-psu isohalines in the Pacific and Atlantic oceans respectively. The Arctic source region is based on geography. To define these regions we used the model's climatology.

The calculated volume fractions last ventilated from each region for the contemporary ACCESS experiments are compared to the corresponding results from DeVries and Primeau (2011) in Table 2. Uncertainty estimates from DeVries and Primeau (2011) are included.

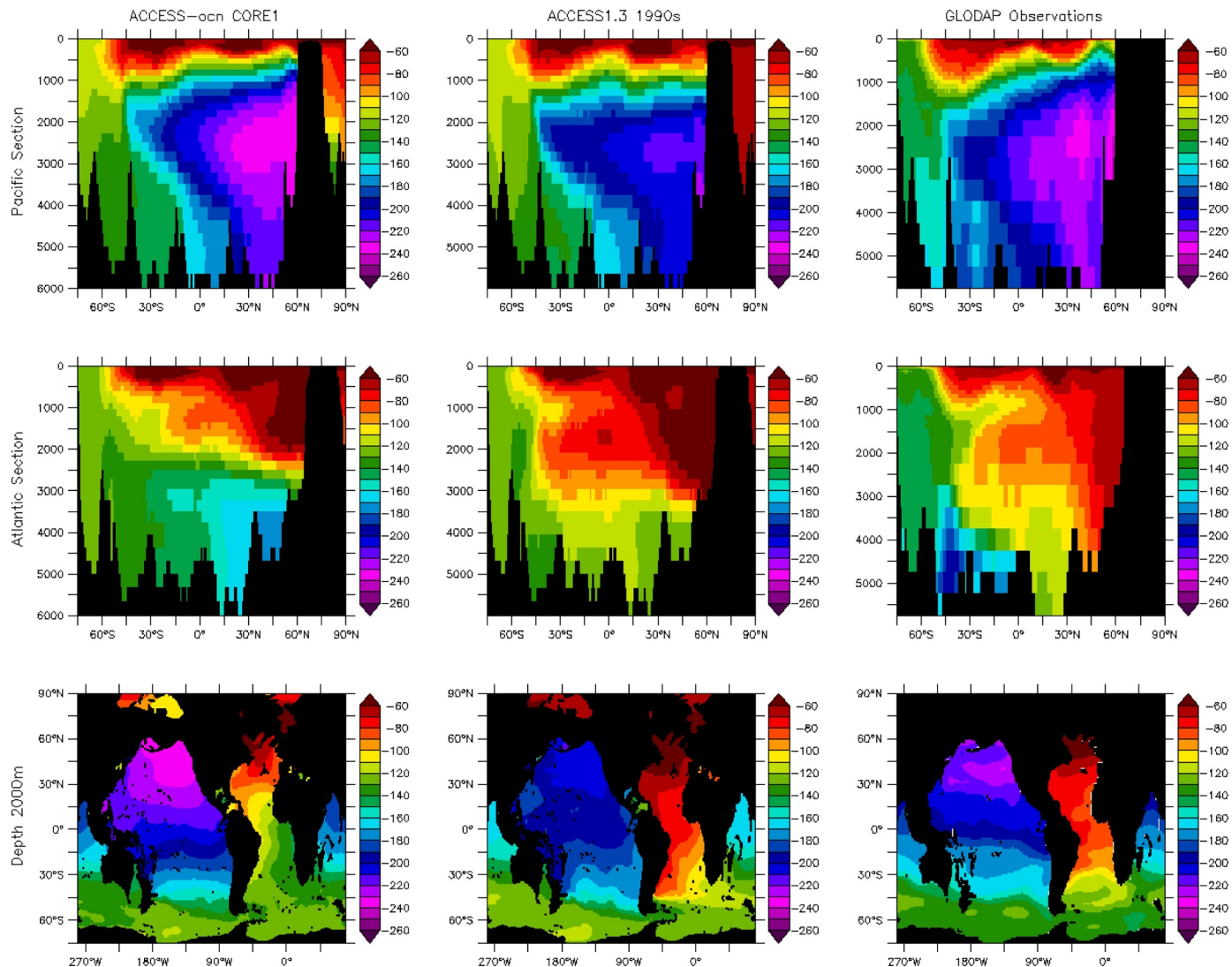


**Fig. 5.** Comparison of radiocarbon solutions (in  $\Delta$ -carbon units) from contemporary ACCESS simulations with observations: ACCESS-ocean with CORE1 forcing (left), ACCESS1.3 historical 1990's circulation (middle), and pre-bomb radiocarbon observations (right, Key et al., 2004). Top row shows Pacific sections ( $180\text{--}190^\circ\text{E}$ ) of  $\Delta$ -carbon, middle has Atlantic sections ( $320\text{--}330^\circ\text{E}$ ) and bottom row shows 2000-m depth slices.

**Table 2**

Percentages of global ocean volumes from regions shown in Fig. 6, calculated from matrix solutions of ACCESS experiments under the contemporary climate, compared with volume fractions from DeVries and Primeau (2011).

Region	ACCESS-ocean	ACCESS1.3 1990	DeVries and Primeau 2011
Arctic	0.3	$1.1 \pm .1$	1
SubArc	12.1	$23.6 \pm .8$	$28 \pm 1$
NthSubTrop	8.0	$12.4 \pm .3$	5
Tropics	3.6	$7.0 \pm .6$	0
SthSubTrop	14.9	$13.8 \pm .2$	10
SubAnt	12.6	$9.5 \pm .3$	$16 \pm 1$
Antarctic	48.5	$32.6 \pm .6$	$40 \pm 3$

Uncertainty from ACCESS experiments are estimated from the range of volume fractions calculated from two 5-year averages of circulation; for the ACCESS-ocean, these ranges were less than the level of significance reported. In all cases, the ocean volume is dominated by water from

Antarctica and the North Atlantic, with only small contributions from the tropics and subtropics. Both ACCESS models underestimate the contribution of water from the subarctic, which includes the North Atlantic Deep Water, though ACCESS1.3 contributions are closer to values of DeVries and Primeau (2011), consistent with the more realistic Atlantic radiocarbon tracers in Fig. 5. Antarctic waters are the largest water mass fraction in all solutions, however, the ACCESS-ocean solution overestimates the contribution relative to DeVries and Primeau (2011) while ACCESS1.3 underestimates.

The volume contributions from tropical and subtropical waters estimated by DeVries and Primeau (2011) are all smaller than for the ACCESS models, with zero contribution reported from the tropics. However, the tropical contributions from our matrix solutions of a few percent are reasonable considering a typical mixed-layer depth of 100 m is a few percent of the water column and the tropics cover a large fraction of the ocean surface. The ACCESS1.3 contributions from the tropics and subtropics are higher than ACCESS-ocean, consistent with the observation of deeper surface mixing in radiocarbon in Fig. 5.

**Table 3**

Percentages of global ocean volumes from regions shown in Fig. 6 from ACCESS1.3 climate projections.

Region	ACCESS1.3 1890	ACCESS1.3 1990	ACCESS1.3 2040	ACCESS1.3 2090
Arctic	1.0	1.1	3.0	3.5
SubArc	21.1	23.6	19.3	20.3
NthSubTrop	11.0	12.4	13.9	15.7
Tropics	7.2	7.0	9.0	11.3
SthSubTrop	14.7	13.8	19.7	25.6
SubAnt	9.8	9.5	11.3	19.9
Antarctic	35.2	32.6	23.8	3.7

### 3.3. Effect of changing climate

We now characterise the response of the ocean circulation to climate change in terms of water-mass fractions and water ages from different phases of the ACCESS1.3 historical and RCP8.5 experiments. Note that tracer fields shown are steady-state solutions to matrices; however, the circulations represented by these matrices are transient and responding to a changing climate. Water ages are very similar from transports from the 1890s (not shown) and the 1990s (left column of Fig. 7); deep North Pacific ages are 1127 and 1189 years respectively, for regions compared in Section 2.2.2. The overall pattern of water age is similar in all climates shown. However, Pacific waters are substantially older for steady states based on future circulations. North Atlantic Deep Water does not penetrate as deep for the future circulation and older water extends further across the Atlantic basin and pools in the abyssal North Atlantic. Note again, that these are steady-state solutions; the mean water age at depth would not have doubled by 2090, but these solutions indicate a halving in the exchange with the upper ocean in the future climate.

Like water age, volume fractions of water masses from the 1890s and the 1990s are very similar (Table 3). In contrast, the volume fractions for the 2090s circulation are quite distinct. (The solution for the 2040s circulation shows the same pattern of changes, but with smaller magnitudes.) The most significant feature of the 2090s circulation is the shutdown in formation of Antarctic Bottom Water; the combined Antarctic regions ventilated 30 to 35% of the global ocean volume in the 1890s and 1990s, which drops to a mere 4% in the 2090s. By contrast, North Atlantic Deep Water contributions to the global volume (the major component of SubArc, Table 3) is relatively

constant. The drop in the Antarctic contribution is compensated by increases in ventilation from all other regions, in particular the subantarctic and southern subtropical regions.

The shutdown of Antarctic Bottom Water can also be seen in Pacific sections of water-mass fractions (Fig. 8). Deep waters of the Southern Ocean, south of 60°S were almost entirely Antarctic water in the contemporary circulation. In the 2090s, Antarctic-ventilated water only penetrates down to a few hundred metres (bottom row). The main change in the extent of subarctic water (which includes North Atlantic Deep Water) is to extend into the Southern Ocean in this Pacific section (top row). The fraction of water from the tropics increases with climate change, though the change is limited (second row). The extent of water from the subantarctic and southern subtropics clearly increases (third and fourth rows), encroaching into the deep ocean and transported across the global ocean.

We emphasise that the ocean state in the 2090s, for example, will not be in steady state. Should the climate of the 2090s be maintained for an extended period (centuries), deep water properties would eventually adjust and Antarctic Bottom Water formation would resume at some timescale, producing circulations different to those presented here.

The weakening of deep circulation in a changing climate has been noted before, both in reviews of CMIP climate projections (e.g., Marsland et al., 2013; Heuzé et al., 2015) and in observations indicative of changes already occurring (de Lavergne et al., 2014). Marsland et al. (2013) show considerable reduction in the Antarctic Bottom Water circulation in the ACCESS1.3 simulations of RCP4.5 and RCP8.5 from early in the 21st century. These circulation changes correspond to decreases in winter mixed-layer depths in Antarctic seas; maximum mixed layers from ACCESS1.3 are up to 5000 m in the Ross and Weddell Seas early in the 21st century, which shoal to a few hundred metres by 2100 for RCP8.5. There is a similar story in the North Atlantic, although the rate of decrease in North Atlantic Deep Water and mixed-layer depth reduces after 2050 here. Heuzé et al. (2015) also find a weakening in the deep circulation and a strengthening in the upper ocean circulation in a survey of CMIP5 projections. de Lavergne et al. (2014) argue that the 1970's Weddell Sea polynya event was a more regular event in the past, and its recent absence is consistent with the observed freshening of the upper Southern Ocean in the current climate. The work presented here highlights this weakening of the deep circulation, showing the dramatic decrease in the contribution of Antarctic waters to the global ocean in projected circulations. This has major implications for the storage of heat and carbon in future climate scenarios.

## 4. Summary and conclusions

The ocean circulations of global climate models are explored using transport matrices, both to compare transport metrics to observations and to demonstrate the effects of changing model climate. Matrices are constructed from standard ocean-model output, specifically, mean volume transport fields and mixed-layer depths, together with empirically determined values for vertical and horizontal diffusivities in the deep and upper ocean that are consistent with parameters of the parent ocean models. This technique does not require any special tracer packages to be run in the forward ocean model. It is therefore possible to build these matrices from archives of ocean and climate simulations. These matrices then provide a numerically highly efficient means for probing various aspects of the transport and biogeochemistry of the parent models.

Correlations between water age solutions from transport matrices and forward models are very high, demonstrating that our matrices capture the parent model's transports with good fidelity. Radiocarbon distributions from the ACCESS-ocean model forced with CORE boundary conditions and the historical ACCESS1.3 experiment both

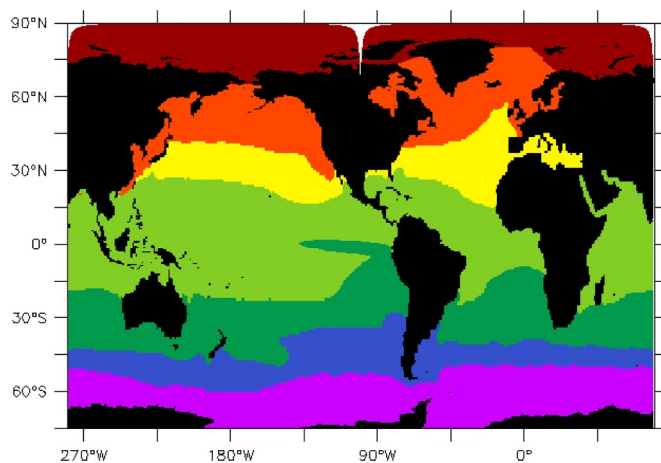
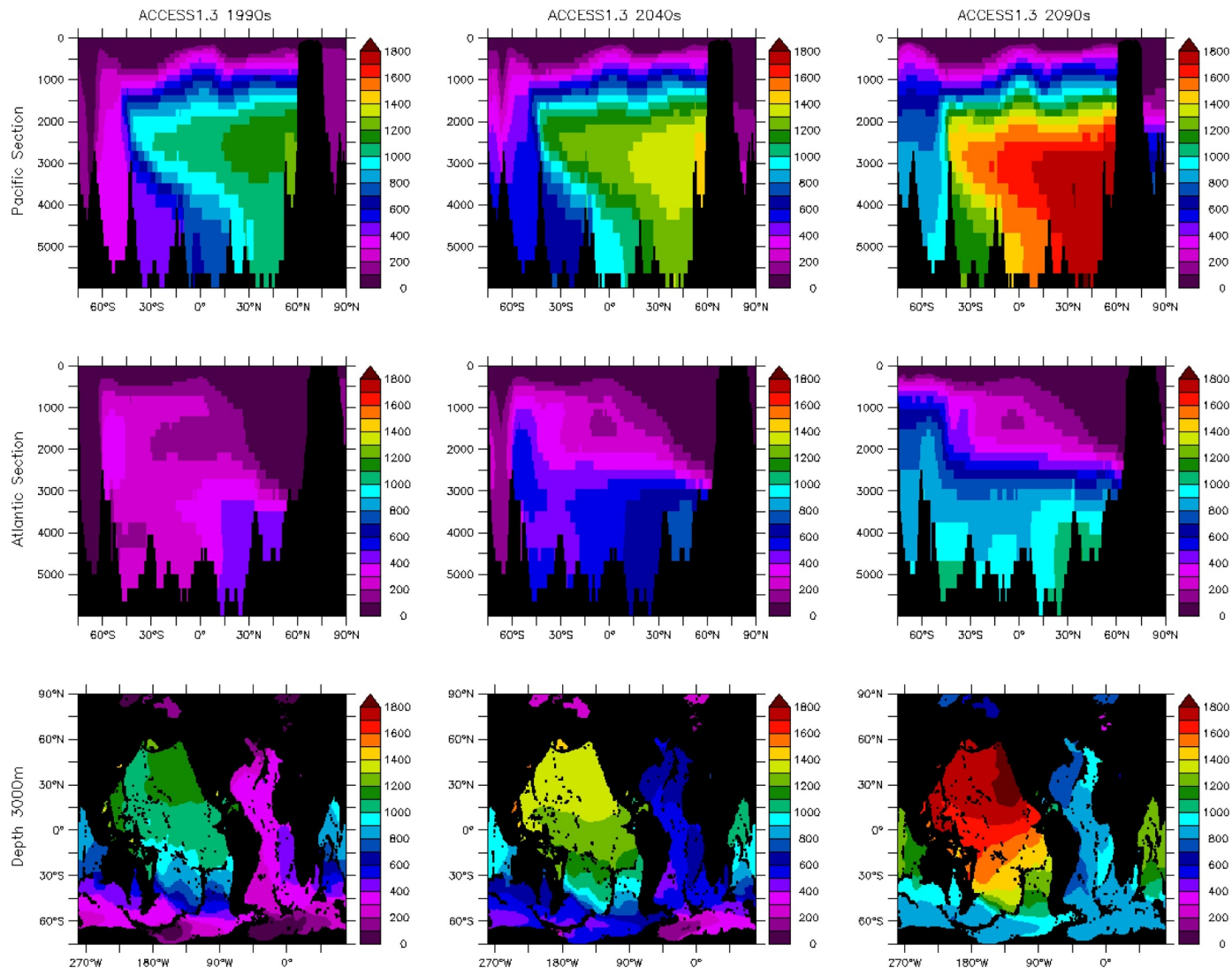


Fig. 6. Map of surface regions used to calculate water mass fractions for the ACCESS experiments, based on regions used by DeVries and Primeau (2011).



**Fig. 7.** Comparison of water age solutions from ACCESS1.3 climate experiments: historical 1990s climate (left), RCP8.5 2040s (centre) and 2090s (right). Top row shows Pacific sections ( $180^{\circ}$ – $190^{\circ}$ E), middle has Atlantic sections ( $320^{\circ}$ – $330^{\circ}$ E) and bottom row shows 3000-m depth slices.

resemble observed fields. Radiocarbon in ACCESS-CORE is closer to observations in the Pacific basin, while ACCESS1.3 gives a better representation in the Atlantic. The ACCESS-CORE based matrix overestimates the volume fraction of the ocean that was last ventilated in Antarctic waters, whereas ACCESS1.3 underestimates this fraction.

Using the transport matrix based on the ACCESS1.3 climate projection for the 2090s under the RCP8.5 scenario, we show an increase in radiocarbon depletion and reduction in the fraction of global ocean last ventilated around Antarctica, pointing to a shutdown in projected Antarctic Bottom Water formation. The radiocarbon fields and water-mass fractions for the 2040s circulation show similar changes to those seen in the 2090s, albeit with smaller amplitudes. The decreased water from Antarctic regions is compensated by an increase in water volume from other regions, in particular from the subantarctic and southern subtropics. Changes in deep circulation are important because they directly affect the ocean's ability to store heat and carbon, which in turn

impacts the future climate including the projected sea level changes.

Future applications of our method to generate transport matrices are numerous. Matrix-derived tracer fields may be used to provide “spun-up” deep-water initial conditions for forward models, greatly reducing the computational expense required to equilibrate these dynamical forward models.

Transport matrices also enable the efficient computation of deep biogeochemical fields, such as the distributions of phosphate, nitrate, dissolved iron, silicic acid and their isotopic ratios, in various climate scenarios. These fields have long timescales and are expensive to integrate exclusively in forward ocean models but can be very efficiently solved for steady state using Newton or Newton-Krylov solvers, or even direct matrix inversion when the source/sink terms are linear as in examples shown here. Being able to efficiently find nutrient and trace-metal distributions will be invaluable for understanding both future and past biogeochemical cycles.

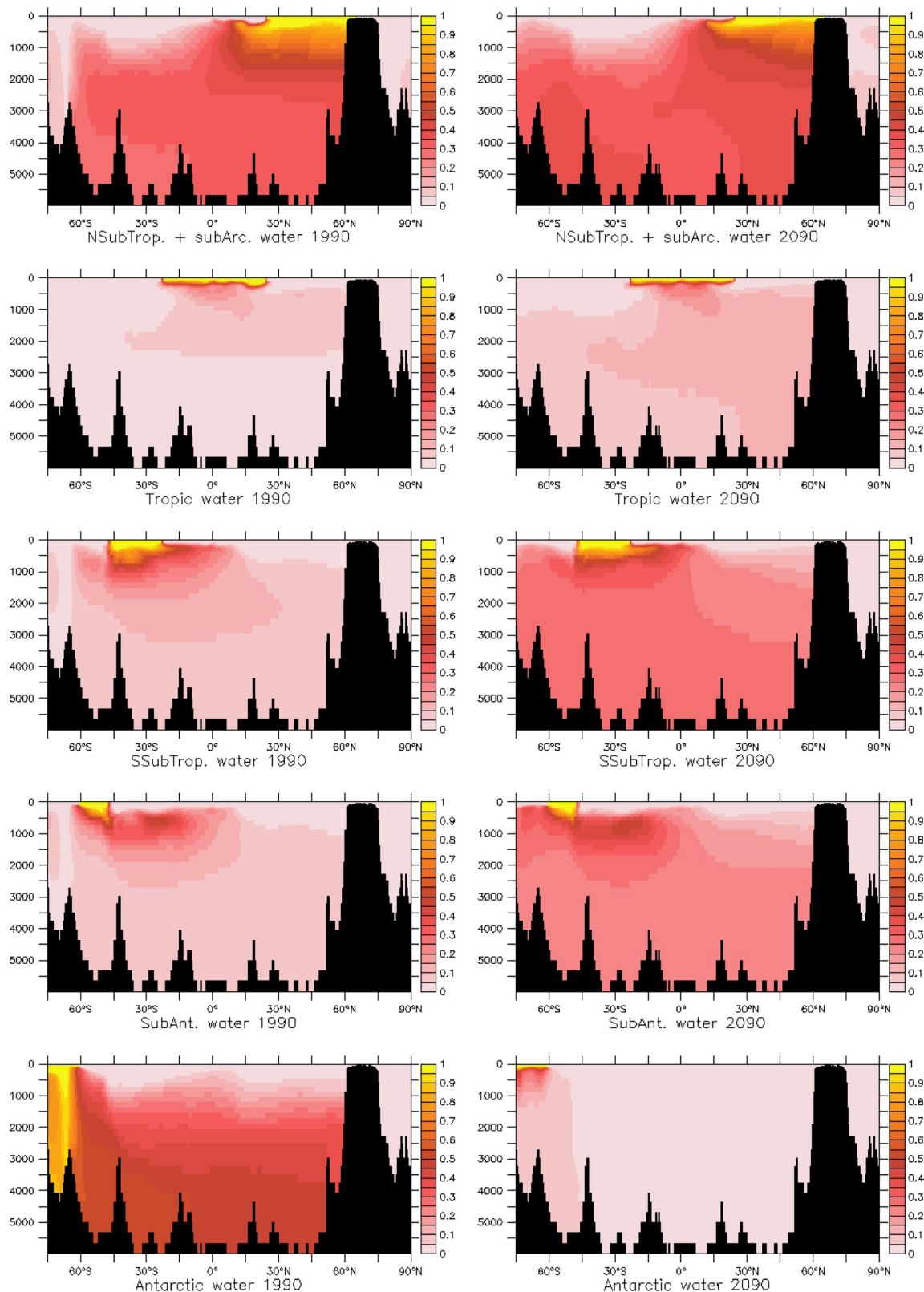


**Fig. 8.** Distributions of water-mass fractions along a Pacific section ( $180\text{--}190^{\circ}\text{E}$ ) for the current climate (left) and projected RCP8.5 climate (right). Water masses plotted are from regions in Fig. 6 and Table 3, including the Antarctic (bottom), up to the combined north subtropical and subarctic regions (top).

## Acknowledgements

This research used computation resources and archives available at the National Computational Infrastructure (NCI), which is located at the Australian National University and supported by the Australian Government. Analyses and graphics in this paper used Ferret, a product of NOAA's Pacific Marine Environmental Laboratory. We also thank the

teams whose work produced the valuable databases such as the World Ocean Atlas and GLODAP. Preparation of this manuscript was supported by the CSIRO Decadal Forecasting Project. ACCESS model development was funded through the Australian Climate Change Science Program (ACCSP). And thank you to the anonymous reviewers whose comments helped improve the manuscript.

## Appendix A. Construction of transport matrix

Sections 2.2.3 and 2.2.4 give an overview of the construction of matrices in this work; the schematics (Fig. A. 1) and paragraphs below give further details. The time tendency of a tracer in a cell is calculated as a function of the tracer in the nearest neighbours due to advection and diffusion, using output from the forward ocean model. When the tracer field is expressed as a vector, this transport and diffusion operator becomes a sparse matrix where the matrix element  $A_{i,j}$  is the component of the time tendency at position index  $i$  due to the tracer concentration at position  $j$ .

The forward model is built on a B-grid (Arakawa and Lamb, 1977); tracer values are defined at cell centres and velocities are assigned at cell corners. Horizontal volume transports are output and averaged from the forward OGCM for cell boundaries ( $\phi^x$  and  $\phi^y$ , shown in Fig. A. 1a). Vertical volume flow rates ( $\phi^z$ ) are found by assuming zero transport through the bottom (or top) boundary, i.e.  $\phi_{i,j,k_{\max}+\frac{1}{2}}^z = 0$ , and from the horizontal divergence using conservation of mass, or “continuity.” The indices  $(i, j, k)$  refer to the Cartesian position of a grid cell in the forward ocean model. Note the vertical index,  $k$ , is positive down, whereas positive vertical transport is up. Thus the vertical flux is obtained from

$$\phi_{i,j,k-\frac{1}{2}}^z = \phi_{i,j,k+\frac{1}{2}}^z + \phi_{i-\frac{1}{2},j,k}^x - \phi_{i+\frac{1}{2},j,k}^x + \phi_{i,j-\frac{1}{2},k}^y - \phi_{i,j+\frac{1}{2},k}^y. \quad (\text{A. 1})$$

The contribution from advection to the time tendency of tracer concentration ( $\chi_{i,j,k}$ ) is shown in Eq. A. 2 and Fig. A. 1a. We use an upwind advection scheme, that is, only the tracer in grid boxes from which flow originates contribute to the tendency. In Eq. A. 2 this is ensured by the max/min functions. The cell volume ( $V_{i,j,k}$ ) converts the convergence of advective flux to a tendency. The tendency term due to the tracer in the cell itself is the total advection out of the cell.

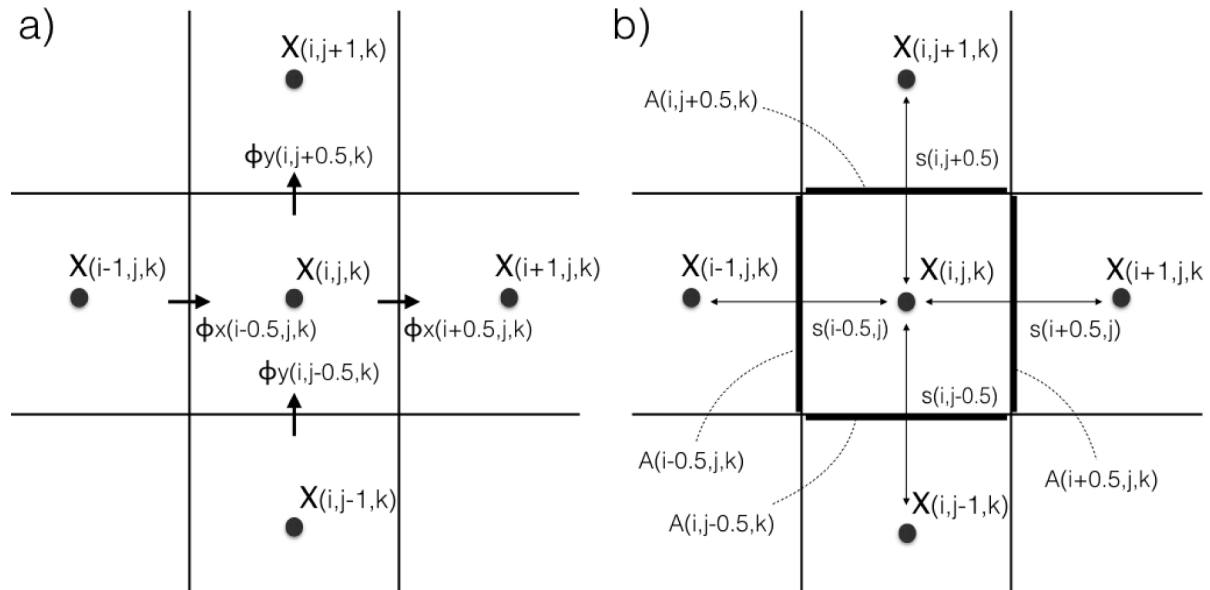


**Fig. A. 1.** Schematic of the grid layout and terms used to calculate the matrix coefficients that give the time tendencies due to a) horizontal advection, and b) horizontal mixing.

$$\begin{aligned}
\frac{d}{dt} \chi_{i,j,k} = & \frac{1}{V_{i,j,k}} [ \\
& \max(0, \phi_{i-\frac{1}{2},j,k}^x) \chi_{i-1,j,k} + \max(0, -\phi_{i+\frac{1}{2},j,k}^x) \chi_{i+1,j,k} + \\
& \max(0, \phi_{i,j-\frac{1}{2},k}^y) \chi_{i,j-1,k} + \max(0, -\phi_{i,j+\frac{1}{2},k}^y) \chi_{i,j+1,k} + \\
& \max(0, \phi_{i,j,k+\frac{1}{2}}^z) \chi_{i,j,k+1} + \max(0, -\phi_{i,j,k-\frac{1}{2}}^z) \chi_{i,j,k-1} + \\
& (\min(0, \phi_{i-\frac{1}{2},j,k}^x) + \min(0, -\phi_{i+\frac{1}{2},j,k}^x)) + \\
& (\min(0, \phi_{i,j-\frac{1}{2},k}^y) + \min(0, -\phi_{i,j+\frac{1}{2},k}^y)) + \\
& (\min(0, \phi_{i,j,k+\frac{1}{2}}^z) + \min(0, -\phi_{i,j,k-\frac{1}{2}}^z)) \chi_{i,j,k} ] \tag{A. 2}
\end{aligned}$$

Similarly, the time tendency due to diffusion is calculated from tracer gradients between nearest neighbouring cells, using  $s$ , the distance between cells, and  $A$ , the area of cell boundaries (shown in Fig. A. 1b and Eq. A. 3). The horizontal diffusivity ( $k^h$ ) is considered constant whereas vertical diffusivity ( $k^z$ ) depends on whether the cells are in the deep or upper ocean. Section 2.2.4 shows results of water age tracer fields found with different combinations of diffusivities, which are compared to age tracer fields from the forward OGCM.

$$\begin{aligned}
\frac{d}{dt} \chi_{i,j,k} = & \frac{1}{V_{i,j,k}} [A_{i-\frac{1}{2},j,k} k^h \frac{(\chi_{i-1,j,k} - \chi_{i,j,k})}{s_{i-\frac{1}{2},j,k}} + \\
& A_{i+\frac{1}{2},j,k} k^h \frac{(\chi_{i+1,j,k} - \chi_{i,j,k})}{s_{i+\frac{1}{2},j,k}} + \\
& A_{i,j-\frac{1}{2},k} k^h \frac{(\chi_{i,j-1,k} - \chi_{i,j,k})}{s_{i,j-\frac{1}{2},k}} + \\
& A_{i,j+\frac{1}{2},k} k^h \frac{(\chi_{i,j+1,k} - \chi_{i,j,k})}{s_{i,j+\frac{1}{2},k}} + \\
& A_{i,j,k-\frac{1}{2}} k^z_{i,j,k-\frac{1}{2}} \frac{(\chi_{i,j,k-1} - \chi_{i,j,k})}{s_{i,j,k-\frac{1}{2}}} + \\
& A_{i,j,k+\frac{1}{2}} k^z_{i,j,k+\frac{1}{2}} \frac{(\chi_{i,j,k+1} - \chi_{i,j,k})}{s_{i,j,k+\frac{1}{2}}} ] \tag{A. 3}
\end{aligned}$$

The gridded, 3-dimensional tracer fields are organised into vectors so that these advective and diffusive terms become coefficients of the transport matrix. The time tendency components from advection and mixing are added together to form the advective-diffusive operator,  $\mathbf{A}$ , that has been applied to tracers in the body of this paper. All tracer solutions solved here are for steady state, hence time-stepping does not need to be considered.

As discussed by Khatiwala et al. (2005), there are several properties of the transport matrix which are useful to check the precision of its construction. For instance, the sum of terms on any row and the volume-weighted sum of terms in any column must be zero. We checked that our matrices satisfy these conservation constraints to within the expected numerical precision.

## References

- Arakawa, A., Lamb, V.R., 1977. Computational design of the basic dynamical processes of the UCLA general circulation model. In: Chang, J. (Ed.), General Circulation Models of the Atmosphere. Methods in Computational Physics: Advances in Research and Applications 17. Elsevier, pp. 173–265. <https://doi.org/10.1016/B978-0-12-460817-7.50009-4>.
- Aumont, O., Orr, J.C., Jamous, D., Monfray, P., Marti, O., Madec, G., 1998. A degradation approach to accelerate transitions to steady state in a 3-D tracer transport model of the global ocean. *Clim. Dyn.* 14, 101–116. <https://doi.org/10.1007/s003820050212>.
- Bardin, A., Primeau, F., Lindsay, K., 2014. An offline implicit solver for simulating pre-bomb radiocarbon. *Ocean Modell.* 73, 45–58. <https://doi.org/10.1016/j.ocemod.2013.09.008>.
- Bardin, A., Primeau, F., Lindsay, K., Bradley, A., 2016. Evaluation of the accuracy of an offline seasonally-varying matrix transport model for simulating ideal age. *Ocean Modell.* 105, 25–33. <https://doi.org/10.1016/j.ocemod.2016.07.003>.
- Bi, D., Dix, M., Marsland, S.J., O'Farrell, S., Rashid, H.A., Uotila, P., Hirst, A.C., Kowalczyk, E., Golebiewski, M., Sullivan, A., Yan, H., Hannah, N., Franklin, C., Sun, Z., Vohralík, P., Watterson, I., Zhou, X., Fielder, R., Collier, M., Ma, Y., Noonan, J., Stevens, L., Uhe, P., Zhu, H., Griffies, S.M., Hill, R., Harris, C., Puri, K., 2013. The ACCESS coupled model: description, control climate and evaluation. *Aust. Meteorol. Oceanogr. J.* 63, 41–64.
- Bi, D., Marsland, S.J., Uotila, P., O'Farrell, S., Fielder, R., Sullivan, A., Griffies, S.M., Zhou, X., Hirst, A.C., 2013. ACCESS OM, the ocean-Sea ice core of the ACCESS coupled model. *Aust. Meteorol. Oceanogr. J.* 63, 213–232.
- Delworth, T.L., Broccoli, A.J., Rosati, A., Stouffer, R.J., Balaji, V., Beesley, J.A., Cooke, W.F., Dixon, K.W., Dunne, J., Dunne, K.A., Durachta, J.W., Findell, K.L., Ginoux, P., Gnanadesikan, A., Gordon, C.T., Griffies, S.M., Gudgel, R., Harrison, M.J., Held, I.M., Hemler, R.S., Horowitz, L.W., Klein, S.A., Knutson, T.R., Kushner, P.J., Langenhorst, A.R., Lee, H.-C., Lin, S.-J., Lu, J., Malyshov, S.L., Milly, P.C.D., Ramaswamy, V., Russell, J., Schwarzkopf, M.D., Sheviakova, E., Sirutis, J.J., Spelman, M.J., Stern, W.F., Winton, M., Wittenberg, A.T., Wyman, B., Zeng, F., Zhang, R., 2006. GFDL's CM2 global coupled climate models. Part I: formulation and simulation characteristics. *J Clim* 19, 643. <https://doi.org/10.1175/JCLI3629.1>.
- DeVries, T., Primeau, F., 2011. Dynamically and observationally constrained estimates of water-mass distributions and ages in the global ocean. *J. Phys. Oceanogr.* 41, 2381–2401. <https://doi.org/10.1175/JPO-D-10-05011.1>.
- Flocco, D., Schroeder, D., Feltham, D.L., Hunke, E.C., 2012. Impact of melt ponds on Arctic sea ice simulations from 1990 to 2007. *J. Geophys. Res. (Oceans)* 117, C09032. <https://doi.org/10.1029/2012JC008195>.
- Frants, M., Holzer, M., DeVries, T., Matear, R., 2016. Constraints on the global marine iron cycle from a simple inverse model. *J. Geophys. Res. (Biogeosci.)* 121, 28–51. <https://doi.org/10.1002/2015JG003111>.
- Fu, W., Primeau, F., 2017. Application of a fast Newton-Krylov solver for equilibrium simulations of phosphorus and oxygen. *Ocean Modell.* 119, 35–44. <https://doi.org/10.1016/j.ocemod.2017.09.005>.
- Gebbie, G., Huybers, P., 2010. Total matrix intercomparison: a method for determining the geometry of water-mass pathways. *J. Phys. Oceanogr.* 40, 1710–1728. <https://doi.org/10.1175/2010JPO4272.1>.

- Griffies, S.M., 2008. Elements of MOM4p1. GFDL Ocean Group Technical Report No. 6. NOAA/Geophysical Fluid Dynamics Laboratory. Code and documentation available online at [www.gfdl.noaa.gov](http://www.gfdl.noaa.gov).
- Griffies, S.M., Biastoch, A., Böning, C., Bryan, F., Danabasoglu, G., Chassignet, E.P., England, M.H., Gerdes, R., Haak, H., Hallberg, R.W., Hazeleger, W., Jungclaus, J., Large, W.G., Madec, G., Pirani, A., Samuels, B.L., Scheinert, M., Gupta, A.S., Severijns, C.A., Simmons, H.L., Treguier, A.M., Winton, M., Yeager, S., Yin, J., 2009. Coordinated ocean-ice reference experiments (COREs). *Ocean Modell.* 26, 1–46. <https://doi.org/10.1016/j.ocemod.2008.08.007>.
- Hadgem2 Development Team, Martin, G.M., Bellouin, N., Collins, W.J., Culverwell, I.D., Halloran, P.R., Hardiman, S.C., Hinton, T.J., Jones, C.D., McDonald, R.E., McLaren, A.J., O'Connor, F.M., Roberts, M.J., Rodriguez, J.M., Woodward, S., Best, M.J., Brooks, M.E., Brown, A.R., Butchart, N., Dearden, C., Derbyshire, S.H., Dharssi, I., Doutriaux-Boucher, M., Edwards, J.M., Falloon, P.D., Gedney, N., Gray, L.J., Hewitt, H.T., Hobson, M., Huddleston, M.R., Hughes, J., Ineson, S., Ingram, W.J., James, P.M., Johns, T.C., Johnson, C.E., Jones, A., Jones, C.P., Joshi, M.M., Keen, A.B., Liddicoat, S., Lock, A.P., Maidens, A.V., Manners, J.C., Milton, S.F., Rae, J.G.L., Ridley, J.K., Sellar, A., Senior, C.A., Totterdell, I.J., Verhoef, A., Vidale, P.L., Wiltshire, A., 2011. The HadGEM2 family of Met Office unified model climate configurations. *Geosci. Model Dev.* 4, 723–757. <https://doi.org/10.5194/gmd-4-723-2011>.
- Heuzé, C., Heywood, K.J., Stevens, D.P., Ridley, J.K., 2015. Changes in global ocean bottom properties and volume transports in cmip5 models under climate change scenarios. *J. Clim.* 28 (8), 2917–2944. <https://doi.org/10.1175/JCLI-D-14-00381.1>.
- Holzer, M., Brzezinski, M.A., 2015. Controls on the silicon isotope distribution in the ocean: new diagnostics from a data-constrained model. *Global Biogeochem. Cycle.* 29, 267–287. <https://doi.org/10.1002/2014GB004967>.
- Holzer, M., Primeau, F.W., 2006. The diffusive ocean conveyor. *Geophys. Res. Lett.* 33, L14618. <https://doi.org/10.1029/2006GL026232>.
- Holzer, M., Primeau, F.W., 2008. The path-density distribution of oceanic surface-to-surface transport. *J. Geophys. Res. (Ocean.)* 113, C01018. <https://doi.org/10.1029/2006JC003976>.
- Holzer, M., Primeau, F.W., 2013. Global teleconnections in the oceanic phosphorus cycle: patterns, paths, and timescales. *J. Geophys. Res. (Ocean.)* 118 (4), 1775–1796. <https://doi.org/10.1002/jgrc.20072>.
- Holzer, M., Primeau, F.W., DeVries, T., Matear, R., 2014. The southern ocean silicon trap: data-constrained estimates of regenerated silicic acid, trapping efficiencies, and global transport paths. *J. Geophys. Res. (Ocean.)* 119, 313–331. <https://doi.org/10.1002/2013JC009356>.
- Key, R.M., Kozyr, A., Sabine, C.L., Lee, K., Wanninkhof, R., Bullister, J.L., Feely, R.A., Millero, F.J., Mordy, C., Peng, T.-H., 2004. A global ocean carbon climatology: results from global data analysis project (GLODAP). *Global Biogeochem. Cycle.* 18, GB4031. <https://doi.org/10.1029/2004GB002247>.
- Khatiwala, S., 2008. Fast spin up of ocean biogeochemical models using matrix-free Newton Krylov. *Ocean Modell.* 23, 121–129. <https://doi.org/10.1016/j.ocemod.2008.05.002>.
- Khatiwala, S., Visbeck, M., Cane, M.A., 2005. Accelerated simulation of passive tracers in ocean circulation models. *Ocean Modell.* 9, 51–69. <https://doi.org/10.1016/j.ocemod.2004.04.002>.
- Kwon, E.Y., Primeau, F., 2006. Optimization and sensitivity study of a biogeochemistry ocean model using an implicit solver and in situ phosphate data. *Global Biogeochem. Cycle.* 20, GB4009. <https://doi.org/10.1029/2005GB002631>.
- de Lavergne, C., Palter, J.B., Galbraith, E.D., Bernardello, R., Marinov, I., 2014. Cessation of deep convection in the open southern ocean under anthropogenic climate change. *Nat. Clim. Chang.* 4 (4), 278–282. <https://doi.org/10.1038/nclimate2132>.
- Marsland, S.J., Bi, D., Uotila, P., Fiedler, R., Griffies, S.M., Lorbacher, K., O'Farrell, S., Sullivan, A., Uhe, P., Zhou, X., Hirst, A.C., 2013. Evaluation of ACCESS climate model ocean diagnostics in CMIP5 simulations. *Aust. Meteorol. Oceanogr. J.* 63, 101–119.
- Pasquier, B., Holzer, M., 2017. Inverse-model estimates of the ocean's coupled phosphorus, silicon, and iron cycles. *Biogeosciences* 14, 4125–4159. <https://doi.org/10.5194/bg-14-4125-2017>.
- Primeau, F., 2005. Characterizing transport between the surface mixed layer and the ocean interior with a forward and adjoint global ocean transport model. *J. Phys. Oceanogr.* 35, 545. <https://doi.org/10.1175/JPO2699.1>.
- Primeau, F.W., Holzer, M., DeVries, T., 2013. Southern ocean nutrient trapping and the efficiency of the biological pump. *J. Geophys. Res. (Ocean.)* 118 (5), 2547–2564. <https://doi.org/10.1002/jgrc.20181>.
- Rhein, M., Rintoul, S.R., Aoki, S., Campos, E., Chambers, D., Feely, R.A., Gulev, S., Johnson, G.C., Josey, S.A., Kostianoy, A., Mauritzen, C., Roemmich, D., Talley, L.D., Wang, F., 2013. Chapter 3: Observations: Oceans. IPCC, 2013: Climate Change 2013: The Physical Science Basis. Cambridge University Press, Cambridge, United Kingdom and New York, NY, USA.
- Ribbe, J., Tomczak, M., 1997. On convection and the formation of subantarctic mode water in the fine resolution antarctic model (FRAM). *J. Mar. Syst.* 13 (1–4), 137–154. [https://doi.org/10.1016/S0924-7963\(96\)00119-4](https://doi.org/10.1016/S0924-7963(96)00119-4).
- Toggweiler, J.R., Dixon, K., Bryan, K., 1989. Simulations of radiocarbon in a coarse-resolution world ocean model: 1. steady state prebomb distributions. *J. Geophys. Res. (Ocean.)* 94, 8217–8242. <https://doi.org/10.1029/JC094iC06p08217>.
- Toggweiler, J.R., Dixon, K., Bryan, K., 1989. Simulations of radiocarbon in a coarse-resolution world ocean model: 2. distributions of bomb-produced carbon 14. *J. Geophys. Res. (Ocean.)* 94, 8243–8264. <https://doi.org/10.1029/JC094iC06p08243>.